Structure of the Stacked Disk Aggregate of Tobacco Mosaic Virus Protein

Rubén Díaz-Avalos and Donald L. D. Caspar
Institute of Molecular Biophysics, Florida State University, Tallahassee, Florida 32306, and Rosenstiel Center, Brandeis University, Waltham, Massachusetts 02154 USA

ABSTRACT The coat protein of tobacco mosaic virus is known to form three different classes of aggregate, depending on environmental conditions, namely helical, disk, and A-protein. Among the disk aggregates, there are four-layer, six-layer, and long stacks, which can be obtained by varying the ionic strength and temperature conditions during the association process. The four-layer aggregate has been crystallized, and its structure solved to atomic resolution. The stacked disk aggregate had been presumed to be built of a polar two-layer disk related to the crystalline A and B rings. A study using monoclonal antibodies specific to the bottom surface of TMV protein demonstrated that the stacked disk aggregate is bipolar, and suggested that the repeating two-layer unit might be similar to the dihedrally symmetrical A-ring pair in the disk crystal. In this paper we present a three-dimensional reconstruction of the stacked disk aggregate obtained by electron microscopy of ice-embedded samples. After modeling of the structure, we found the ring pairs to have the same quaternary structure as the A-ring pair of the four-layer aggregate. The resolution achieved in the image processing of the electron micrographs is on the order of 9 Å in the meridional direction and 12 Å in the equatorial. The identification of the structure of the stacked disk with the A-ring pair of the disk crystal provides an explanation of the observation that the axial periodicity of the disk pair, which is ~53 Å when fully hydrated, can shrink to ~43 Å in the dry state.

INTRODUCTION

The existence of a protein in the extracts of plants infected with tobacco mosaic virus (TMV) was detected in the early 1950s (Commoner et al., 1953). The observation that this protein was not associated with RNA caused it to be classified as a nonvirus protein, although it was known to be immunologically related to TMV protein, and to polymerize into rods similar to those of TMV.

In the first reported x-ray patterns of this "abnormal" protein polymer (Franklin and Commoner, 1955), it was noted that the axial periodicity could vary by more than 20%, according to the water content, whereas the spacings in TMV remain constant, regardless of the hydration state. In dry fibers, the axial spacing for this protein was observed to be 6% lower than the helix pitch spacing of TMV, and upon addition of water, these meridional layer lines shifted toward the center of the pattern, corresponding to spacings up to 15% larger than in the virus. This suggested that the structure of the "abnormal" protein was somewhat similar to the structure of the helical protein assembly in the virus, although it was more loosely held together. The existence of meridional layer lines at spacings slightly more than twice that of the TMV helix pitch was attributed to a pairing of cyclic protein aggregates. The variation in the periodicity of the rods was postulated to be caused by the intercalation of two monolayers of water between neighboring rings. This polymorphic arrangement of TMV protein was later named the "stacked disc" (Klug and Caspar, 1960).

Because the stacked disk and helical assemblies can be obtained together from polymerized A-protein (consisting mostly of trimers), an equilibrium between the two forms was surmised (Caspar, 1963). The presumed switching between the stacked-disk and helical aggregates implied that the stacked disk, like the virus helix, should be a polar structure, with the layers of subunits all pointing in the same direction. This assumption was supported by a 3D reconstruction obtained by electron microscopy (Unwin and Klug, 1974; Unwin, 1974). The name "disc" was changed to "disk" (Butler and Klug, 1971) when the polar two-layer aggregate was hypothesized to act as the initiator of virus assembly. The pairing observed in the x-ray patterns of the stacked disk (Finch and Klug, 1974) was presumed to arise from a perturbation akin to the periodic perturbation previously observed in the dahlemense strain of TMV (Caspar and Holmes, 1969), where turns of the protein helix are brought alternately closer together and further apart on one side of the virus particle.

The deduction of the polarity of the stacked disk from electron micrographs of negatively stained samples was based on the difference in the cross-correlation of images computed for opposite orientations (Unwin and Klug, 1974; Unwin, 1974). The differences observed, although small, were regarded as significant. Reanalysis of similar images (Kuhn and Caspar, unpublished observations) indicated that the departures from dihedral symmetry were on the order of the noise level in the micrographs; thus the electron microscope images were not incompatible with a bipolar structure for the stacked disk.

Received for publication 5 May 1997 and in final form 15 September 1997.

Address reprint requests to Dr. Rubén Díaz-Avalos, Institute of Molecular Biophysics, Florida State University, Tallahassee, FL 32306. Tel.: 850-644-3275; Fax: 850-561-1406; E-mail: diaz@sb.fsu.edu; URL: http://www.sb.fsu.edu/~diaz.

0006-3495/98/01/595/09 $2.00

A definite proof of the bipolarity of the stacked disk was provided by a study undertaken using electron micrographs of stacked disks decorated with a class of monoclonal antibodies prepared by immunization with TMV protein (Dore et al., 1990). These antibodies had been identified as being specific for an epitope present on protein subunits on disk aggregates and on one end of the viral rods (Dore et al., 1988). The epitope was found to be on the surface of the protein that contains the left and right radial α-helices, called the "bottom" (Champness et al., 1976).

Electron micrographs of negatively stained monoclonal antibody reacted with stacked disks show antibody molecules bound at both ends of the stacked disk rods (Dore et al., 1990), proving that the stacked disk is a bipolar aggregate. Binding of antibodies to both ends of the stacked disk was observed, regardless of the number of two-layer units that were present in a rod. Because every stacked-disk rod seemed to be formed by identical two-layer units, this observation suggested that every two-layer unit should be bipolar, and that every two-layer unit is held together by symmetrical contacts at the "top" surface, that is, the surface spanned by the left- and right-slewed α-helices. Given the close relationship of the stacked disk and the crystalline four-layer disk (Bloomer et al., 1978), it was then natural to expect the two-layer unit of the stacked disk to be very similar to the central, dihedrally connected A-ring pair of the four-layer aggregate (Caspar and Namba, 1990).

In this paper we present a three-dimensional reconstruction of the stacked-disk aggregate, obtained by cryoelectron microscopy of frozen hydrated samples and image processing, as well as some molecular modeling, which shows that, to the resolution attained here, the disk pairs forming the stacked disk closely resemble the A-ring pair of the disk crystal.

MATERIALS AND METHODS

Protein preparation

TMV (common strain) was purified from infected tobacco plants by several cycles of differential centrifugation. The protein was extracted from the virus by the modified acetic acid degradation method of Scheele and Lauffer (1967). Briefly, two volumes of ice-cooled glacial acetic acid were added to 20 ml of 2% TMV solution. The precipitated RNA was removed by 10 min of centrifugation (10,000 $\times$ g) at 4°C. The acetic acid was then removed by using a gel filtration column (G-25 Sephadex) equilibrated with 0.1% acetic acid, and the protein was collected as 15-ml fractions in tubes containing 100 mM phosphate buffer (pH 7.5), in which the protein precipitated. The protein was then pelleted by 10 min of centrifugation (20,000 $\times$ g) and resuspended with 100 mM KCl. It was then stored in the helical form in 0.1 M sodium acetate buffer at pH 4.6. To prevent bacterial contamination, 1 mM sodium azide was added to the protein stock.

For the assembly of the protein into stacked disks, the protein was dialyzed at 4°C into 0.1 M Tris, pH 8, for 24 h. This was followed by dialysis into 0.2 M ammonium sulfate, 0.1 M Tris, at pH 8.0 for 3 days, with four changes of buffer. After the third day, the flask containing the protein and buffer was brought to room temperature. The precipitate formed during the high salt dialysis was removed by centrifugation at 6600 $\times$ g for 15 min. Under these conditions, the sedimentation constants for the predominant components of the stacked disks are ~38S, 45S, and 52S (Raghavendra et al., 1985), corresponding to 6-, 8-, and 10-layer aggregates. The stacked disks were made longer by aggregation in an acidic buffer, and the sedimentation constant became greater than 100S. Measurements of the sedimentation constants were carried out in a Beckman model E analytical ultracentrifuge.

Electron microscopy of ice-embedded specimens

The samples were prepared for electron microscopy by placing a 4-μl drop of sample, at a concentration of 1.0 mg/ml, on a holey grid that was previously glow-discharged in air for ~2 min. Then the drop was blotted with filter paper and plunged into ethane slush.

The grids were observed at the Rosenstiel Center, using a Philips CM12 TEM microscope equipped with a Gatan anticontaminator; a Gatan cryoholder was used to mount the grids. Low-dose images were taken at a magnification of 45,000×, with a 30-μm objective aperture, using an accelerating voltage of 100 kV. We aimed for a defocus close to but lower than 4500 Å, so that the fourth meridional layer line would fall inside the first node of the contrast transfer function (CTF) (Erickson and Klug, 1971).

IMAGE ANALYSIS

The individual micrographs were selected before scanning with an optical diffractometer to discard the ones that showed specimen drift, astigmatism, or excessive defocus. For the reconstruction we used two micrographs that showed layer lines beyond 12 Å spacing, and which had ~10 usable particles each, that is, particles that were straight, did not intersect any others, and were more than 3000 Å long (see Fig. 1). For the present reconstruction, we used 16 particles, with ~60 disk pairs each, giving a total of ~32,000 protein subunits.

The film was digitized for image processing with a Perkin-Elmer PDS-1010M densitometer at the Institute of Molecular Biophysics, using a raster size of 15 μm, which translates into a sampling of 3.33 Å per pixel on the digitized image.

Helical symmetry

After the filament images were straightened out using a spline fitting algorithm (Egelman, 1986), we proceeded to determine the symmetry of the particles. For this purpose, we measured the spacing of the first meridional layer line

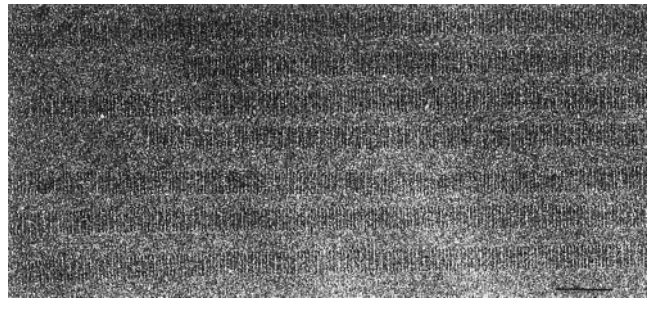

FIGURE 1 Electron micrograph of ice-embedded stacked disks. There are seven 180-Å-diameter particles horizontally aligned in the field of this micrograph. The thickness of each disk layer is 26.8 Å. The image was taken at 4500 Å underfocus and 45,000× magnification.

(J_0), which corresponded to a spacing of 53.6 ± 0.16 Å. The first nonmeridional layer line was weak, and therefore the measurement of its spacing was somewhat unreliable. However, there was another nonmeridional layer line that showed strongly in the power spectrum, corresponding to a spacing of ~76 Å. The ratio of the meridional position of this layer line to the position of the first J_0 term came out to be 0.701 ± 0.006. These values are very close to the values for the layer line positions from x-ray patterns of oriented stacked disk fibers observed by Finch and Klug (1974), and therefore we will use the indexing provided in that paper.

According to the indexing, the layer line located at a spacing of 76.4 Å corresponds to a Bessel order of 17 and is the seventh layer line. The ratio of 0.701 for the meridional position of the seventh to the tenth layer lines means that the ratio of the position of the third layer line to the first, J_0, is 0.299. Because of the 17-fold symmetry of the particles, this ratio corresponds to the steepest 17-start helix, which in the stacked disk corresponds to the lowest nonzero Bessel order possible. The twist angle is given, then, as $(0.299 \times 2\pi)/17$, that is, 6.33°. Thus there is very nearly an axial repeat of 536 Å, corresponding to 10 disk pairs.

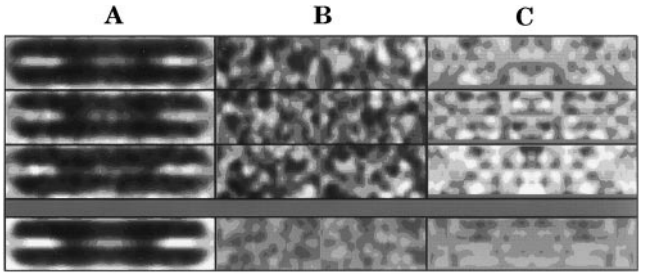

FIGURE 2 Disk-pair average images and asymmetrical noise. The top three rows are translational averages and asymmetrical differences of disk-pair images from three selected particles, and the bottom row is the average of these three. Column A shows the translationally averaged disk-pair images corresponding to the projection of the cylindrically averaged structure, which should be bilaterally symmetrical if noise-free. Column B shows the left-right difference of the translational average, which is a measure of noise in the image. Column C shows the top-bottom difference of the translational average, averaged left and right to impose cylindrical symmetry. The top-bottom differences in Column C are generally smaller than those in Column B, indicating that any polarity in the disk-pair structure is less than the asymmetrical noise level in these images. Increasing the number of images averaged (last row) reduces the noise level, enhancing the apparent dihedral symmetry of the disk pair.

Polarity and noise

To determine if the images showed any evidence of polarity, we first obtained a translational average of all of the disk pairs in each particle image, which corresponds to obtaining a projection of the cylindrical average of the disk pairs. Indeed, the layer lines for the translational period of the disk pairs are all the J_0 terms. Because the repeat period is very close to 10 disk pairs with 17-fold symmetry, the first nonzero Bessel function contributing to these layer lines is J_{170}, which would only be significant at spacings beyond 3 Å; thus to our resolution, the translational average coincides with the projection of the cylindrical average.

Once the translational average was obtained, an estimation of the level of noise was made from the asymmetry between the left and right sides of the image. Ideally, there must be mirror symmetry between the left and right sides of a cylindrical average; however, because of the presence of noise in the images, the translational average will show differences in the right-hand side as compared to the left-hand side. These deviations provide a natural estimate of the level of noise in the images. Thus the noise level is indicated by the left-right difference of the translationally averaged disk pairs, as shown in the central column of Fig. 2.

For a polar particle, the up-down difference of the cylindrical average is dependent on the degree of polarity. Therefore, we computed the left-right average of each of the disk pairs, which corresponds to the best representation of the true cylindrical average, and then the up-down difference. Thus we see that the up-down difference (Fig. 2, *column C*) is smaller than the level of noise measured in the left-right difference. The comparison in Fig. 2 demonstrates that the power of any polarity present in the filament images must be smaller than the level of noise. From these images we cannot measure any statistically significant polarity, implying that the structure is compatible with dihedral symmetry.

Three-dimensional averaging

As we proceeded with the image processing, the first round of particle averaging was computed by following the procedure of DeRosier and Moore (1970). The images were apodized to minimize edge effects; then the Fourier transform was calculated and the layer line data collected. The phases were corrected for displacement of the phase origin off the helical axis and for tilting of the particle out of the plane normal to the direction of view. Image processing was carried out with the MRC programs for processing of particles with helical symmetry. We collected layer line data up to 9 Å spacing in the meridional direction.

To compute an average of the layer line data collected without imposing dihedral symmetry, a particle was chosen randomly to be used as the reference in the first round of alignment (as done by Unwin and Klug, 1974). All of the others were brought to that orientation for averaging by using the data of layer lines 3, 7, 10, 20, and 40. A "Bessel" filter was used for the off-meridional layer lines during alignment; that is, considering that the particles have a radius of ~90 Å, the data of the layer lines with Bessel order ±17 should be negligible for radial spacings smaller than 0.033 $Å^{-1}$. Likewise, the data for the layer lines with Bessel order ±34 should be negligible for $R \leq 0.066$ $Å^{-1}$. The image transform beyond 9-Å resolution was also filtered out because there were no detectable data above the noise level. After this average was obtained, the process was repeated twice, using as reference the last average obtained.

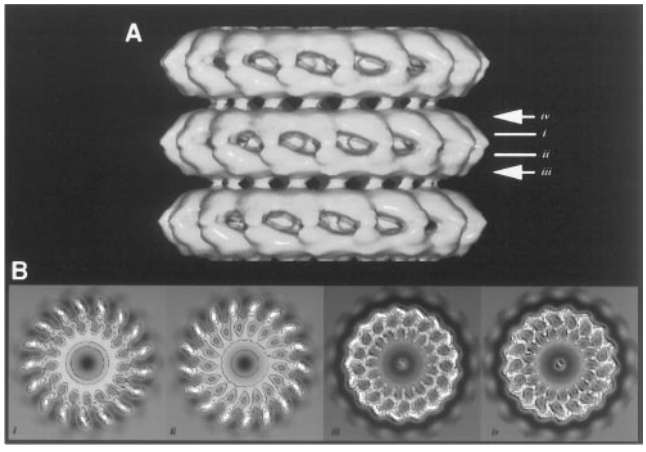

FIGURE 3 (*A*) Surface view of the 3D reconstruction calculated without imposing dihedral symmetry. (*B*) Orthogonal sections through the reconstruction: sections *i* and *ii* were taken at positions corresponding to the slewed a-helices; *i* was taken above the twofold axis (center of the image in *A*), whereas *ii* comes from below the twofold axis. Sections *iii* and *iv* correspond to the region of the radial α-helices, with *iii* coming from below the twofold axis and *iv* from above it.

By computing a 3D map from the layer line data, without imposing dihedral symmetry, one can see that the bipolarity of the structure is a rather clear feature. From sections taken above and below what seems to be a twofold axis, it is seen that the features of the reconstruction change handedness upon crossing the plane containing the evident twofold axes (Fig. 3).

To test if the three-dimensional data possess dihedral or polar symmetry, phase residuals were calculated (table 1) using as the phase origin one of the putative twofold axes in the middle of a two-layer disk of the particle average. This was done by shifting the phase origin to minimize the power of the imaginary component of the average layer line data. The layer lines whose imaginary component was minimized in this case were the 3rd, 7th, 13th, and 17th, which are the strongest nonmeridional layer lines. This minimization selects the best twofold phase origin.

Once we had the average oriented with the best twofold axis as the phase origin, we took four approaches to averaging the data, using this reoriented average as the reference, namely:

1. Alignment and averaging without doing anything extra, i.e., we just did a fourth cycle of alignment and averaging.

2. Stripping the reference of its imaginary component, i.e., using a centrosymmetrical reference for alignment and computing a new particle average.

3. Moving each particle so that it was as close as possible to being centrosymmetrical (by minimizing the power of each particle's imaginary component), stripping each particle of its imaginary component, and then aligning it against the reference oriented to a twofold phase origin, that is, aligning centrosymmetrical data versus a polar reference.

4. Same as above, but using only the real part of the reference for alignment, that is, centrosymmetrical particles were aligned using a centrosymmetrical reference.

The correlation of the data and the reference, as indicated in Table 1, was closer in 4 (16.4° ± 5.8°), than in 3 (24.7° ± 5.6°), than in 2 (29.7° ± 6.9°), and least in 1 (36.2° ± 7°), as can be seen from the phase residuals obtained in each case (cf. Amos and Klug, 1975).

The fact that imposing the dihedral symmetry on the reference improves its correlation with the data (as in 2) indicates that there is no correlation of the data with the

TABLE 1. Phase residuals* for different averages

Particle	Near, up	Far, up	Near, down	Far, down	CR[#]	RD[§] vs PR[¶]	RD vs CR
2562_1	31.3	33.8	30.9	38.4	27.3	25.2	22.6
2562_2	29.4	32.1	27.4	37.0	24.7	22.1	20.7
2562_3	36.7	40.1	38.0	46.5	34.5	30.3	22.6
2562_4	35.1	42.8	39.6	51.4	36.0	31.7	23.4
2562_5	37.8	39.9	45.3	38.4	35.4	28.9	17.7
2562_6	27.9	30.7	25.1	34.8	22.9	18.2	7.1
2562_7	33.2	32.0	38.7	28.6	23.7	17.5	11.8
2562_8	35.5	29.6	32.5	22.5	22.1	18.3	10.6
2562_9	40.4	38.5	45.3	32.9	33.8	27.7	20.0
2561_1	37.1	39.2	43.4	35.0	31.1	24.1	14.3
2561_2	27.3	35.3	29.3	39.8	27.6	22.5	15.1
2561_3	45.2	44.4	53.3	39.6	43.4	32.9	23.2
2561_4	37.9	48.7	43.4	56.8	42.1	35.0	24.0
2561_5	25.1	37.4	31.0	40.3	25.3	22.1	9.3
2561_6	29.7	34.2	37.9	27.5	27.0	22.0	12.7
2561_7	27.2	33.7	26.2	36.1	19.4	16.8	8.3
Average	33.5 ± 5.4	37.0 ± 5.1	36.7 ± 7.9	37.8 ± 8.3	29.7 ± 6.9	24.7 ± 5.6	16.4 ± 5.8

*Phase residuals are in degrees. The first four columns correspond to four different orientations of the averaged polar image used as reference in comparison to the individual particle images.

[#]CR, Centrosymmetrical reference.

[§]RD, Real component of data.

[¶]PR, Polar reference (see text).

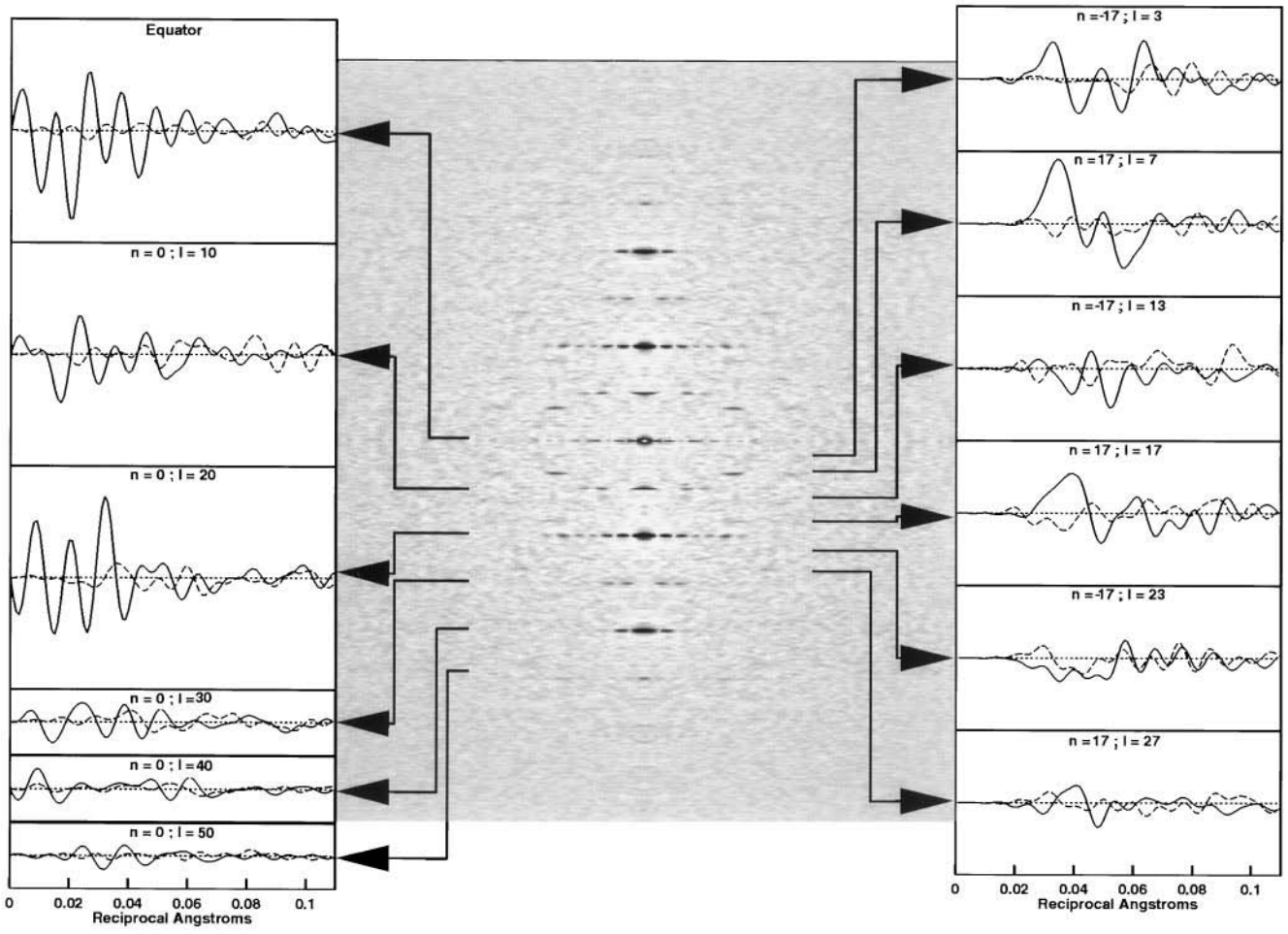

FIGURE 4 Layer line data of the reconstruction, separated into real (*solid lines*) and imaginary (*dashed lines*) components. The diffraction amplitudes, weighted by the radius in reciprocal space, were obtained from the calculated average Fourier transform of 16 stacked disk particles. Helical symmetry was imposed in averaging the off-equatorial layer lines, but dihedral symmetry, which would have eliminated the imaginary parts of the transform, was not imposed. The layer lines in the grayscale display of the calculated average diffraction pattern are indexed to the corresponding plots of the weighted amplitudes.

imaginary component of the average. Likewise, a further improvement in the correlation is obtained when the data are stripped of their imaginary component, because the power of the imaginary component of each particle appears to be pure noise. Therefore, removing some of the noise from the data improves the cross-correlation. Further improvement results when centrosymmetrical data and a centrosymmetrical reference are used. Thus the imaginary components of the Fourier transforms of the data are uncorrelated, which fits the definition of pure noise.

The presence of the imaginary component in the Fourier transforms of the images is useful for determining the spacings at which we still have statistically significant signal. As the resolution of the data increases, the ratio of the imaginary to the real component increases. Beyond the resolution at which the mean amplitudes of these components are equal, the transform is dominated by noise in the image and there are no statistically measurable data. Thus we can see from Fig. 4 that the equator contains significant data to spacings on the order of 12 Å, whereas the 27th layer line, for example, contains significant data to ~14-Å radial spacing.

MODEL BUILDING

The reconstructed surface view of the stacked disk, calculated without imposing dihedral symmetry or correcting for the contrast transfer function (Fig. 3), resembles the corresponding image of the A-ring pair of the four-layer disk crystal derived from the x-ray structure (Bloomer et al., 1978; Bhyravbhatla et al., 1998) and is clearly different from the image of the polar A-B ring pair. Removing the asymmetrical noise from the reconstructed image enhances the correspondence with the crystallographic model of the A-ring pair.

To build a model of the stacked disk to compare with the experimental data, we took the coordinates of the A-ring

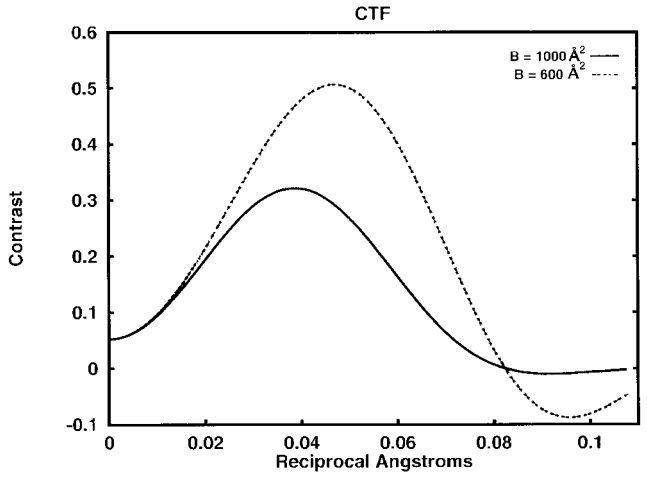

FIGURE 5 Plot of the contrast transfer function corresponding to an amplitude contrast of 4%, a defocus of −4500 Å, and temperature factors of 1000 Å^2 (*solid line*) and 600 Å^2 (*dashed line*). The solid line corresponds to the CTF used to fit the data and model in the radial direction, whereas the dotted line corresponds to the CTF used for the meridional direction. The only difference between the two curves is the temperature factor applied.

pair α-carbon atoms from the disk crystal (Bloomer et al., 1978; Bhyravbhatla et al., 1998) and constructed a filament by imposing the experimentally determined helical symmetry. Then the model filament structure was projected onto a plane parallel to the helical axis. The image thus obtained was treated as another micrograph.

Scattering due to the presence of the solvent was modeled by assuming that the solvent has a uniform density. The scattering of the protein embedded in solvent will be equal to the scattering of the protein in a vacuum, plus the scattering of the solvent surrounding the protein. According to Babinet's principle (Jackson, 1980), this is the same as the scattering of the protein in a vacuum, minus the scattering of solvent displaced by the volume occupied by the protein. We used the values for the volumes of the amino acid residues provided by Zamyatnin (1972) to correct the low-resolution protein model amplitudes for the displaced solvent.

In any optical system, the aperture, aberrations, and diffraction have the effect of blurring a point into an object that is not a point (an Airy disk, for example) (Born and Wolf, 1980). This blurring is described by means of the point spread function, which depends solely on instrumental characteristics. In electron microscopy it is customary to work with the Fourier transform of the point spread function, which is known as the contrast transfer function (CTF). However, in what follows we will incorporate into the CTF the blurring caused by sources other than instrumental. Thus, whereas an ideal CTF is not attenuated, the effects of blurring of the images, caused by disorder in the particles or by defects in the image processing and instrumental limitations such as incoherence, are represented in our modeling of the image transforms by applying a temperature factor to the CTF used for correction.

To compare the model with the electron microscopy data, one has to deal with the problem of the CTF, either by correcting the data by division or by multiplication of the model Fourier transform by the CTF. We decided that the better approach was to multiply the model transform by the CTF, as we would not introduce the problems of incrementing the noise in the neighborhood of the CTF nodes. The first step in dealing with the CTF is to estimate the microscope defocus (Toyoshima and Unwin, 1988; Frank, 1996). The presence of a Thon ring in the Fourier transform of the images gave an estimate of ~4000 Å underfocus for the two micrographs. However, in addition to the amount of defocus, the contrast transfer function of the microscope is determined by the amount of amplitude contrast and the effective temperature factor.

To put the amplitudes on the layer lines corresponding to data and model on the same scale, we used an initial CTF corresponding to the parameters of the microscope, with the experimentally observed underfocus, a null temperature factor, and an estimated amplitude contrast of 5%. We first rescaled the first subsidiary maximum on the equator of the model transform to fit the data. The shape of the curve in the low-resolution region is strongly dependent on the amount of amplitude contrast; therefore, we varied this parameter to obtain a matching shape of the low-resolution region for the equatorial data and model curves. Next we adjusted the temperature factor, so as to have the model equatorial amplitudes decaying in the same way as the data.

Once the equatorial data seemed reasonably approximated by the Fourier transform of the A-ring pair model multiplied by the adjusted CTF, we checked to see whether the same parameters would work adequately in the meridional direction. However, the temperature factor applied to the CTF in the radial direction turned out to be a little too strong for the meridional data, and we had to reduce it to obtain an optimum fit. The CTF parameters that best fit the model transform to the observed data are an underfocus value of 4500 Å, with an amplitude contrast of 4%, and an anisotropic temperature factor of 1000 Å^2 in the radial direction and 600 Å^2 in the meridional direction. A plot of the CTF is shown in Fig. 5.

To make the modeled equatorial transform fit the equatorial data closely, it was necessary to include a small radial contraction factor of 3% for the layer lines of the data; that is, the Fourier transform of the averaged stacked disk image appeared to be shrunk with respect to the model transform scaled to fit the measured axial repeat period. This radial adjustment was necessary to make the nodes of the equators coincide for data and model. The contraction in reciprocal space corresponds to a 3% radial expansion of the particles in real space.

We can only speculate about the significance of the radial scaling that was necessary to make the equators of data and model coincide. This distortion could be due to a small radial expansion of the frozen hydrated stacked disk rods, or to a slight elliptical flattening of the cylindrical rods in the thin ice layer. Nevertheless, the axial periodicity of our

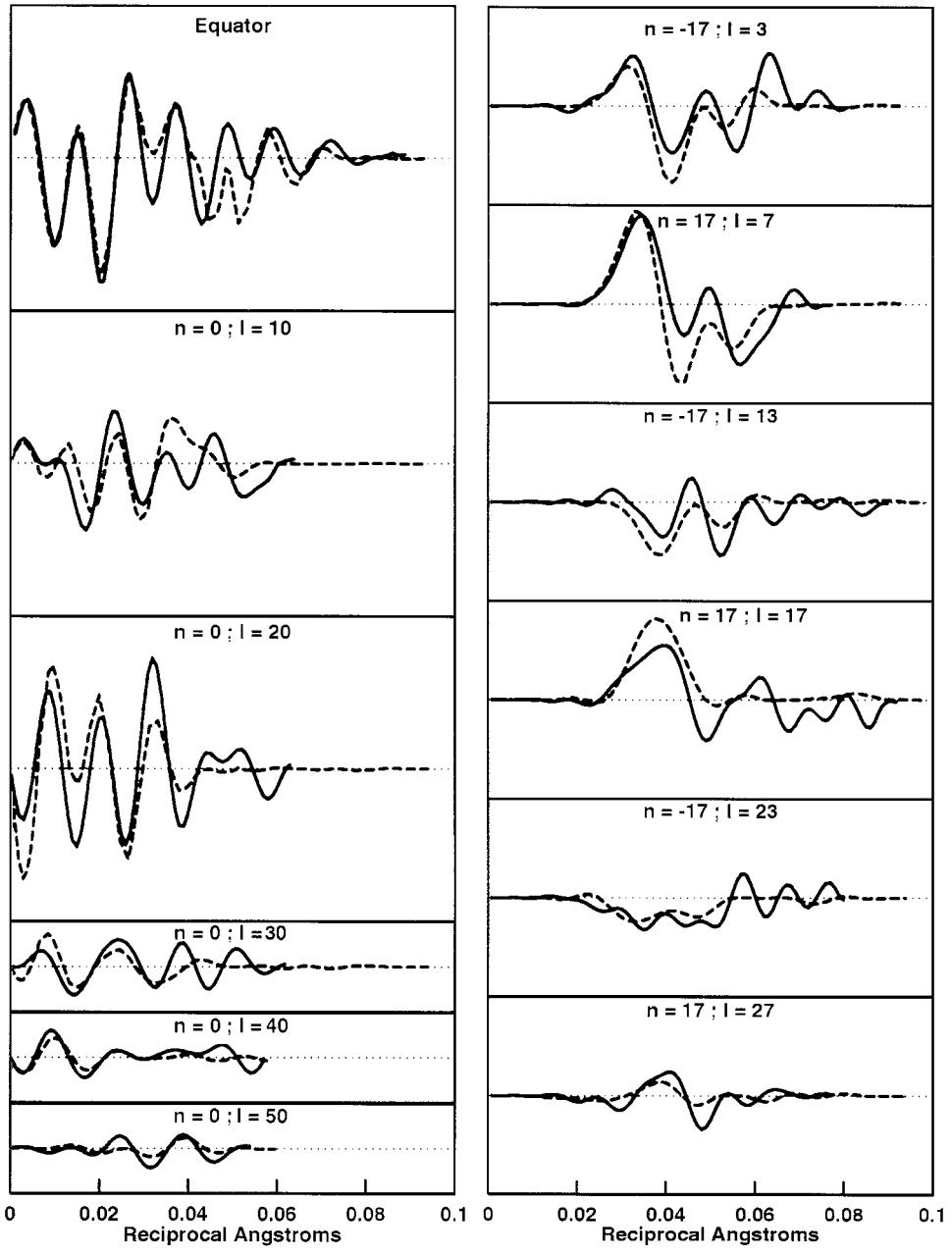

FIGURE 6 Layer lines of data and model. The layer-line amplitudes from the cryomicroscopy data are plotted with solid lines; the CTF-adjusted model transforms, calculated from the atomic structure of the crystalline A-ring pair, are dashed. Only the real part of the experimental layer lines is plotted, as the imaginary component represents noise. There is generally close agreement between model and data to ~20-Å resolution. At higher resolution, fringe positions remain correlated, although there are some differences in amplitudes.

frozen hydrated stacked disk specimens, determined from the microscope magnification, corresponds closely to that measured by x-ray diffraction from an oriented liquid-crystalline sample (Finch and Klug, 1974), which indicates no significant distortion in the axial direction.

Comparison of model and data

As can be seen from Fig. 6, the calculated amplitude on layer lines of the model corrected for the effective CTF closely follows the experimental data, although there are some discrepancies. For example, the equatorial plot shows a very good fit to spacings of ~20 Å. Even though the amplitudes are not exactly the same for most of the layer lines, the overall behaviors of the curves of data and model are very similar, in the sense that they have their extreme points at the same position, with the phases coinciding for the most part.

The phase residual for the alignment of the data and the CTF-corrected model is 17.5°, which indicates a very good

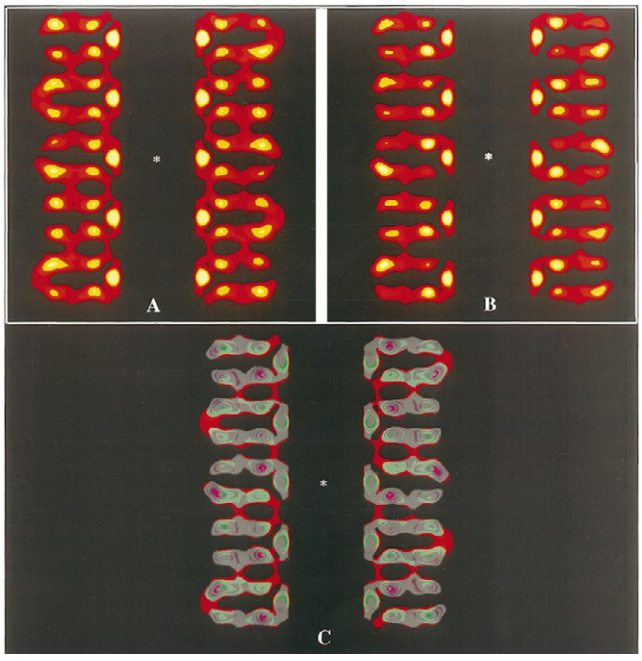

FIGURE 7 Axial section through the image reconstruction of the stacked disk and the model based on the crystalline A-ring pair. The section cuts through five disk pairs along the axis of the assembly, with a twofold axis (*) perpendicular to the plane of the section. Succeeding sections of the stack are related by in-plane horizontal dyads bounding this five-disk-pair segment. Because the level of noise in the reconstructed density map was estimated to be on the order of 25% of the peak densities, we display four levels, each corresponding to the magnitude of the standard deviation of the average density. *A* is a section obtained from the experimental data, and *B* is the corresponding section of the modeled stacked disk rod, convoluted with the experimental point spread function of the electron micrographs, using the same color table as in *A*. *C* is the superposition of *A* and *B* with the color table of *B* inverted. The grey areas denote complete agreement of the two structures, whereas reddish regions denote dominance of the experimental data, and bluish shades indicate where the model is stronger. The differences between the data and model are on the order of the standard deviation of the experimentally averaged densities.

correlation. This phase residual is, in fact, comparable to that comparing the centrosymmetrically averaged data to the real components of the individual particle transforms (Table 1), which provides a measure of the residual noise in the reconstructed image. Computation of a crystallographic *R*-factor comparing data and model yields $R = 0.21$, which is another demonstration that the model based on the atomic structure of the A-ring pair fits the reconstructed image within the noise level of the electron microscopy data.

Large discrepancies between the data and model would be attributable to regions of the protein having a conformation different from that of the modeled one. If this were the case, a real-space difference map of data minus model would show negative peaks in the regions where the model has densities that do not exist in the data, and positive peaks where the data has densities that do not exist in the model. A difference map computed by Fourier inversion of the layer lines corresponding to data minus model did not show structurally interpretable differences between data and model.

Discrepancies between model and data may also be due to crudeness of the modeling procedure, such as the solvent correction that was used, or to subtle differences between the pair of rings that build the stacked disk and the crystalline A-ring pair model. A real-space comparison of the model with the data demonstrates that the correspondence between them is quite close. Fig. 7d) shows a central section through a 3D filament with five disc pairs, oriented so that a twofold axis is at the center of the figure (marked by the *asterisk*). Because of the particle symmetry, the axial section shows five different sections of the disk pairs, which correspond to 10 different views of the protein subunit; that is, the figure contains sections of the protein subunit sliced every 2.1°. Superposition of the reconstructed stacked disk and model images (Fig. 7 *C*) demonstrates that the statistically significant features coincide.

The 6.33° helical twist between disk pairs, which leads to the axial repeat consisting of 10 dihedral disk pairs with 17-fold rotational symmetry, generates twofold axes perpendicular to the particle axis spaced 1.05° apart in projection. It is this bristling array of dyads that makes all of the orthogonally projected views of the stacked disk rods centrosymmetrical. The centrosymmetry of the projections has facilitated accurate estimation of the noise from the antisymmetrical components of the image transforms, and has enhanced the reliability of the image averaging. With averaging of more cryomicroscopy images, it would be possible to obtain a more detailed comparison of the stacked-disk pair structure than with that of the crystalline A-ring pair.

CONCLUSION

We have shown that, to the resolution of our electron image data, the stacked disk consists of two-layered disk units that have the same packing arrangement and overall conformation as the A-ring pair of the four-layer disk crystal.

Based on the crystal structure (Bloomer et al., 1978), it was previously thought that the A-ring pairs of the four layers were held together by a quadrupole interaction between Lys^{53} and Glu^{22} with their corresponding counterparts across the dyad axis (Caspar and Namba, 1990). However, a new refinement of the disk crystal structure (Bhyravbhatla et al., 1998) shows that the interactions across the dyad axis in the four-layer aggregate are mediated through bound water molecules, and that there are no direct protein-protein contacts across the major overlapping surfaces. In the stacked disk, there must be a dihedrally paired, water-mediated connection between the slewed α-helical surfaces ("top-to-top" pairing) similar to that in the crystalline A-ring pair. Presumably, the symmetrical contacts between the radial α-helical surfaces ("bottom-to-bottom" pairing) in the stacked disk, which have no homology in the crystalline four-layer aggregate, also involve water-mediated linkages similar to those of the "top-to-top" surface pairing. The symmetrical connections between the radial α-helical surfaces may be more tenuous than those

observed crystallographically for the dihedral pairing of the slewed α-helical surfaces, because the EM images show lower density at the "bottom-to-bottom" boundary of the disk pairs.

The evidence that the fully hydrated stacked disk is formed by water-linked A-ring pairs provides an explanation of the observation made more than 40 years ago by Franklin and Commoner (1955), which showed that the stacked-disk axial periodicity depended strongly on water activity. Lowering the water activity resulted in the removal of water molecules from the interfaces of the disk pairs, causing the axial periodicity of the stacked disk to shrink from ~53 Å to ~43 Å.

A disk aggregate was thought to play a special role in the assembly of virus particles (Butler and Klug, 1971). This hypothesis was based on the principle of quasiequivalence (Caspar and Klug, 1962), making a self-consistent story in which the pieces of evidence all seemed to fit together. Even the stacked disk, which did not play a central role in the hypothesized assembly process, could be viewed as surplus nucleating aggregate that assembled into harmless rods. Nevertheless, if disk aggregates have no biological role to play in viral assembly, the existence of the crystalline four-layer disk was a lucky break that helped the elucidation of the structure of the protein in the virus.

It is interesting to note that after observing the water dependency of the stacked disk axial periodicity, Franklin and Commoner (1955) inferred that this structure was a rather frail one. However, the stacked disk turns out to be the most stable polymer formed by TMV protein, as shown by persistance of this aggregate after extensive treatment under depolymerizing conditions (Raghavendra et al., 1985, 1986), thus becoming a dead end for the TMV coat protein association.

We thank Marguerite Cahoon for help with most of the biochemistry, as well as Amy McGough, Teresa Ruiz, and Jean Luc Rank for helpful discussions.

This work was supported by U. S. Public Health Service Research grant 5R35CA47439 to DLDC from the National Cancer Institute.

REFERENCES

Amos, L. A., and A. Klug. 1975. Three dimensional image reconstructions of the contractile tail of T4 bacteriophage. *J. Mol. Biol.* 99:51–73.

Bhyravbhatla, B., S. Watowich, and D. L. D. Caspar. 1998. Refined atomic model of the four-layer aggregate of the tobacco mosaic virus coat protein at 2.4 Å resolution. *Biophys. J.* 74: 604–615.

Bloomer, A. C., J. N. Champness, G. Bricogne, R. Staden, and A. Klug. 1978. Protein disk of tobacco mosaic virus at 2.8 Å resolution showing the interactions within and between the subunits. *Nature.* 276:362–368.

Born, M., and E. Wolf. 1980. Principles of Optics. Pergamon Press, Elmsford, NY.

Butler, P. J. G., and A. Klug. 1971. Assembly of the particle of tobacco mosaic virus from RNA and disks of protein. *Nature New Biol*. 229: 47–50.

Caspar, D. L. D. 1963. Assembly and stability of the tobacco mosaic virus particle. *Adv. Protein Chem*. 18:37–121.

Caspar, D. L. D., and K. C. Holmes. 1969. Structure of dahlemense strain of tobacco mosaic virus: a periodically deformed helix. *J. Mol. Biol.* 46:99–133.

Caspar, D. L. D., and A. Klug. 1962. Physical principles in the construction of regular viruses. *Cold Spring Harb. Symp. Quant. Biol.* 27:1–23.

Caspar, D. L. D., and K. Namba. 1990. Switching in the self assembly of tobacco mosaic virus. *Adv. Biophys.* 26:157–185.

Champness, J. N., A. C. Bloomer, G. Bricogne, P. J. G. Butler, and A. Klug. 1976. The structure of the protein disk of tobacco mosaic virus to 5 Å resolution. *Nature.* 259:20–24.

Commoner, B., M. Yamada, S. Rodenberg, T. Want, and E. Basler. 1953. The proteins synthesized in tissue infected with tobacco mosaic virus. *Science.* 118:529–534.

DeRosier, D. J., and P. B. Moore. 1970. Reconstruction of three dimensional images from electron micrographs of structures with helical symmetry. *J. Mol. Biol.* 52:355–369.

Dore, I., C. Ruhlmann, P. Oudet, M. Cahoon, D. L. D. Caspar, and M. V. H. Van Regenmortel. 1990. Polarity of binding of monoclonal antibodies to tobacco mosaic virus rods and stacked disks. *Virology.* 176:25–29.

Dore, I., E. Weiss, D. Altschuh, and M. H. V. Van Regenmortel. 1988. Visualization of the location of tobacco mosaic virus epitopes reacting with monoclonal antibodies in enzyme immunoassay. *Virology.* 162: 279–289.

Egelman, E. 1986. An algorithm for straightening images of curved filamentous structures. *Ultramicroscopy.* 19:367–373.

Erickson, H., and A. Klug. 1971. Measurement and compensation of defocusing and aberrations by Fourier processing of electron micrographs. *Philos. Trans. R. Soc. Lond. Biol.* 261:105–118.

Finch, J. T., and A. Klug. 1974. The structural relationship between the stacked disk and helical polymers of tobacco mosaic virus protein. *J. Mol. Biol.* 87:633–640.

Frank, J. 1996. Three-Dimensional Electron Microscopy of Macromolecular Assemblies. Academic Press, San Diego.

Franklin, R. E., and B. Commoner. 1955. X-ray diffraction by an abnormal protein (B8) associated with tobacco mosaic virus. *Nature.* 175: 1076–1077.

Jackson, J. D. 1980. Classical Electrodynamics. John Wiley and Sons, New York.

Klug, A., and D. L. D. Caspar. 1960. The structure of small viruses. *Adv. Virus Res.* 7: 1–38.

Raghavendra, K., M. L. Adams, and T. M. Schuster. 1985. Tobacco mosaic virus protein aggregates in solution: structural comparison of 20S aggregates with those near conditions for disk crystallization. *Biochemistry.* 24:3298–3304.

Raghavendra, K., D. M. Salunke, D. L. D. Caspar, and T. M. Schuster. 1986. Disk aggregates of tobacco mosaic virus protein in solution: electron microscopy observations. *Biochemistry.* 25:6276–6279.

Scheele, R. B., and M. A. Lauffer. 1967. Acid-base titrations of tobacco mosaic virus and tobacco mosaic virus protein. *Biochemistry*. 6:3076–3081.

Toyoshima, C., and P. N. T. Unwin. 1988. Contrast transfer for frozen hydrated specimens: determination from pairs of defocussed images. *Ultramicroscopy.* 25:279–291.

Unwin, P. N. T. 1974. Electron microscopy of the stacked disk aggregate of tobacco tosaic virus protein. II. The influence of electron irradiation on the stain distribution. *J. Mol. Biol.* 87:657–670.

Unwin, P. N. T., and A. Klug. 1974. Electron microscopy of the stacked disk aggregate of tobacco mosaic virus protein. I. Three dimensional image reconstruction. *J. Mol. Biol.* 87:641–656.

Zamyatnin, A. 1972. Protein volume in solution. *Prog. Biophys.* 24: 107–123.